JMEPEG (2018) 27:4364–4371
https://doi.org/10.1007/s11665-018-3504-6

©ASM International
1059-9495/$19.00

Investigation of the Performance of Flow Models for TWIP Steel

Suleyman Kilic, Fahrettin Ozturk, and Catalin R. Picu

(Submitted March 13, 2017; in revised form March 27, 2018; published online July 10, 2018)

Modeling of metal processing requires constitutive laws able to represent the experimental material behavior. Of the large number of available empirical constitutive equations, only a subset may be fitted accurately to given experimental data. The present work is aimed at identifying the equations that can be used to model the ambient temperature mechanical behavior of high Mn twinning-induced plasticity (TWIP) steels. These are fitted to experimental data for TWIP900 and further compared in terms of their ability to predict springback. The reference springback value is determined experimentally for the same material. The study provides guidelines for the selection of the constitutive model in forming simulations for this type of steel.

Keywords empirical constitutive equations, finite element analysis, twinning-induced plasticity (TWIP)

1. Introduction

In recent years, the automotive industry has paid more attention to lightweight design, fuel economy, low emissions and vehicle safety. Achieving these goals requires the use of new materials with larger specific strength and energy absorption. Steels play a central role in manufacturing in many industries, including the automotive industry. The new generation of advanced high strength steels (AHSS), including dual-phase (DP), transformation-induced plasticity (TRIP) and twinning-induced plasticity (TWIP) steels, provide large strength, excellent ductility and large energy absorption before failure (Ref 1). The use of lightweight alloying elements in these steels, such as Al, leads to substantial density reduction, with an associated significant increase in the specific strength and toughness (Ref 2).

TWIP steels have austenitic, single-phase structure, which is metastable in ambient conditions. Deformation leads to the nucleation and growth of a large density of twins which, in turn, causes pronounced strain hardening through the dynamic Hall–Petch effect (Ref 3). The large strain hardening associated with the intense twinning stabilizes plastic flow and postpones strain localization such that strains to failure above 30% and true ultimate tensile strengths above 1 GPa are measured (Ref 4-6). The very large specific energy absorbed before failure makes these materials ideals for car frame components with role in energy dissipation during collision (Ref 1, 7).

The key component of TWIP steels is Mn which helps stabilize the face-centered cubic austenitic structure at room temperature (RT). About 27% Mn is required in the binary Fe-Mn system to produce RT metastable austenite. The addition of only 0.6% C reduces the amount of Mn needed for austenite stabilization to about 12%. Increasing the carbon percentage above 1% causes precipitation of carbides, which is not desirable in these alloys. The presence of C reduces the stacking fault, which promotes planar slip. However, in Fe-Mn-C alloys with stacking fault energy (SFE) below 15 mJ/m^2, martensitic transformation (ε-martensite) takes place during deformation leading to the TRIP effect. The addition of Al inhibits the $\gamma - \varepsilon$ martensitic transformation, hence promoting the TWIP effect (Ref 7-10).

The control of the SFE is central to TWIP steel design. Al increases the SFE and so does Si. In general, a SFE in the range 15-40 mJ/m^2 is considered ideal for TWIP (Ref 11). SFE values in this range can be obtained for various material compositions.

Together with the benefits related to the high strength and ductility, the drawback of a large springback during processing of sheet metal emerges (Ref 4, 5). This is usually mitigated by a trial-and-error experimental approach which requires dies to be manufactured and subsequently adapted to minimize springback. However, this procedure is expensive and time-consuming. An alternative is the use of models for the forming process which are able to predict the amount of springback of the part being formed. This allows more precise die design and substantial cost reduction. For optimal performance, these models require as input a constitutive description which reproduces the mechanical behavior of the respective material. Obviously, the constitutive model has a strong influence on the predicted behavior (Ref 12-22). Similarly, the prediction of the forming limit diagram by computational means depends to a large extent on the accuracy of the constitutive model (Ref 23).

The capability of several material models to represent the mechanical behavior of TWIP900 steel is studied in this work. Eight empirical models are fitted to the stress–strain curves obtained experimentally at RT, and their ability to capture the details of the stain hardening versus strain curve is analyzed. Each of these models is then implemented in a commercial finite element package and used to predict the springback for a specific die configuration. The parameters of the yield surface

Suleyman Kilic, Department of Mechanical Engineering, Ahi Evran University, 40200 Kirsehir, Turkey; **Fahrettin Ozturk**, TAI - Turkish Aerospace Industries, Inc., 06980 Ankara, Turkey; and **Catalin R. Picu**, Department of Mechanical, Aerospace and Nuclear Engineering, Rensselaer Polytechnic Institute, Troy, NY 12180. Contact e-mail: suleymankilic@ahievran.edu.tr.

used in the simulation are also calibrated based on experimental data. The reference springback is obtained experimentally using a die setup identical to that used in simulations. It is concluded that five of the eight models considered can be fitted accurately to the experimental data and predict springback with an error smaller than 10%. The results reported can be used to guide material model selection in process simulations of this material.

2. Material and Experimental Procedures

TWIP900 steel sheet of 1.3 mm thickness was used in this study. The material was produced by cold rolling and was supplied by POSCO Steel-Making Company, South Korea. The chemical composition of this steel is Mn (20.96%), Al (4.8%), Cr (0.46%), Cu (0.06%), Si (0.17%), C (0.37%) and Fe (balance). This is a typical TWIP steel composition with high Mn content and added Al to control the stacking fault energy.

The material was used in as-received conditions, and prior heat treatments applied are not known. In order to gain insight into the state of the microstructure, the surface of untested samples was polished and etched with HNO_3 + HCl + water (4:4:2). The Nital solution is generally used to evidence the microstructure of TWIP steels (Ref 24-30). HCl was added in some cases to the Nital solution (Ref 31-33). This combination was selected in this work. Austenite, ε-martensite and α'-martensite are identified based on their color, as they appear after etching as blue/brown, bright and black, respectively (Ref 34, 35). The microstructure was observed by optical and scanning electron microscopy (SEM). Figure 1(a) shows the SEM image of the as-received material. The grain size is approximately 4 μm. Twins of thickness of approximately 800 nm are evidenced by etching. The width of one of the twins is shown by arrows in Fig. 1(a). These large twins span the entire grain and end at grain boundaries. This is a typical microstructure for as-received TWIP (Ref 2, 3, 6). Due to the limited resolution, it was not possible to observe twins of smaller thickness which, however, are a expected to exist (Ref 6).

Tensile test samples were prepared according to the ASTM E8 standard. Tensile tests were performed using a Shimadzu Autograph AGS-X 100 kN tensile testing machine integrated with a video extensometer. Three strain rates of 8.33×10^{-3}, 4.16×10^{-2} and 1.66×10^{-1} s^{-1} were used in separate experiments. Each test was repeated at least three times in order to insure data repeatability. All tests were performed at the ambient temperature.

In order to determine the springback of the material, rectangular plates of dimensions 35 mm × 200 mm were cut with the longitudinal direction in the rolling direction and were deformed using the setup shown schematically in Fig. 2. The device is a 60°V-shaped open die. Bending tests were conducted at 25 mm/min speed and RT. This deformation speed corresponds to an effective maximum strain rate in the outer fibers of the bent beam of 2.1×10^{-3} s^{-1}. No ironing force was used. After bending, the punch was retracted immediately to the starting position. All tests were repeated at least three times, and the resulting stress–strain curves were averaged. Springback was measured by image analysis after unloading.

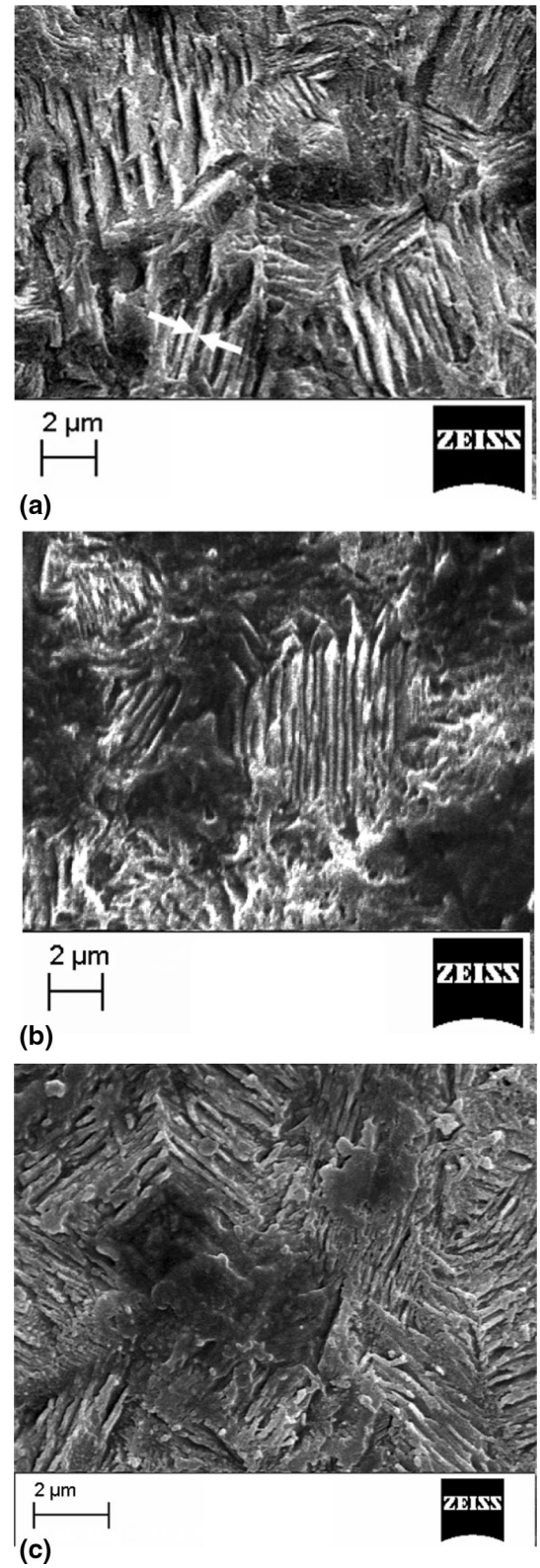

Fig. 1 Scanning electron microscopy images of (a) undeformed (0% strain) and deformed samples at (b) 20% strain and (c) 40% strain. The arrows in (a) show one of the twins and indicate its thickness

3. Constitutive Models Considered

The objective of this study is to test the adequacy of various standard empirical constitutive models to represent the mechanical behavior of TWIP steel.

A large number of such equations have been proposed and used in the literature for various materials. Those considered in this study are presented in Table 1. The list includes some of the most widely used models of this type. In all cases stress depends on strain as the only variable and hence the constitutive behavior is strain rate and temperature insensitive. It is well documented that TWIP has very small strain rate sensitivity (Ref 6-8), which may become slightly negative in certain strain rate and temperature conditions. This is supported by our experimental data discussed in the next section. Due to this reason, we do not include strain rate effects in this analysis. Temperature is important in some applications, especially if strain localization leading to adiabatic shear banding takes place (Ref 36). Localized deformation-induced heating notwithstanding the importance of temperature variations depends on the application. For example, if the material is used in car frames for the purpose of energy dissipation during impact, the temperature variation is not an important design parameter. More importantly, the stacking fault energy increases monotonically with temperature (Ref 9) and this has a strong effect on the TWIP effect. It is possible to completely eliminate the TWIP effect and revert to standard dislocation-based plastic deformation by simply increasing the temperature by few hundred degrees. Due to this reason, most studies of TWIP steels are performed at RT.

All models except Hollomon's, model (1), correspond (as shown in Table 1) to the rigid plastic approximation and are fitted to the post-yield part of the stress–strain curve. The equations in Table 1 include a number of constants which are determined by fitting the material point behavior to the experimental true stress–true strain curves. This is performed using the Levenberg–Marquardt nonlinear optimization technique within the OriginLab software (Ref 37). An overall error of 10^{-6} was imposed as convergence criterion. Multiple starting points were selected during optimization to explore the existence of multiple possible solutions. In cases in which the procedure led to different solutions, that corresponding to the best fit of the experimental data was selected.

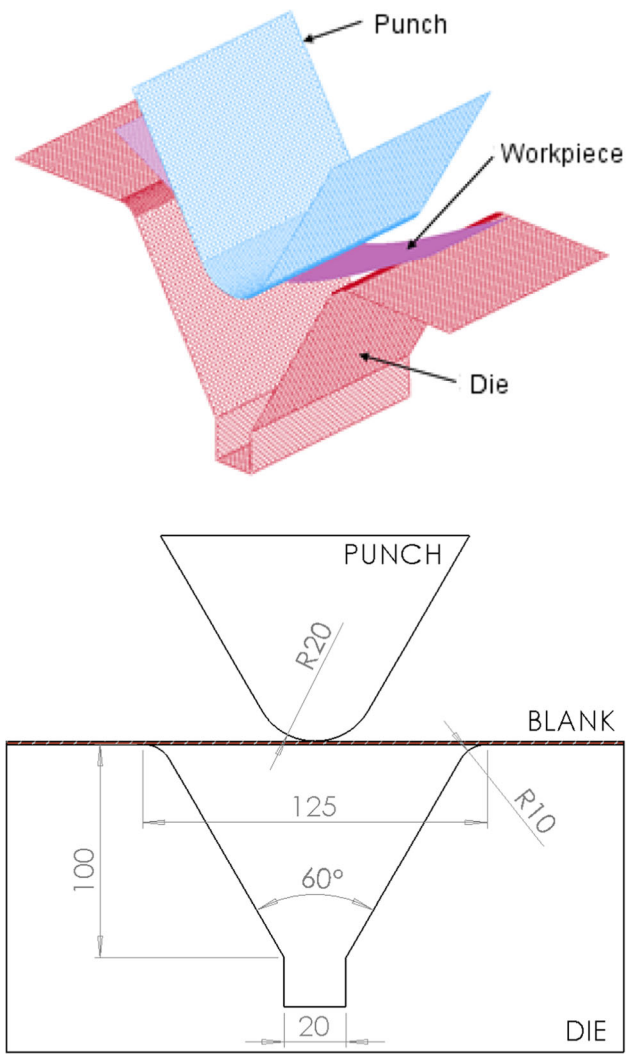

Fig. 2 Setup used for springback evaluation

4. Results and Discussion

4.1 Comparison of Various Constitutive Models

Figure 3 shows the experimental true stress–true strain curves obtained at three strain rates of 8.33×10^{-3}, 4.16×10^{-2} and 1.66×10^{-1} s^{-1}. The curves are typical for this material, exhibiting a weakly rate sensitive yield stress of approximately 600 MPa, and strong and sustained strain hardening. The failure true stress is above 1 GPa, and the failure strain is approximately 35%. The strain rate sensitivity of the flow stress is essentially negligible at all strains. These data are presented in order to support our choice of strain rate-

Table 1 Constitutive models used in this study (Ref 21)

Models	Equations	
Hollomon (Ref 22)	$\sigma(\varepsilon) = A_1\varepsilon^{A_2}$	(1)
Power (Ludwik) (Ref 23)	$\sigma(\varepsilon) = A_1 + A_2\varepsilon^{A_3}$	(2)
Krupskowsky (Swift) (Ref 24)	$\sigma(\varepsilon) = A_1(A_2 + \varepsilon)^{A_3}$	(3)
Voce (Ref 25)	$\sigma(\varepsilon) = A_1 + (A_2 - A_1)\exp(-A_3\varepsilon)$	(4)
Hockett/Sherby (Ref 26)	$\sigma(\varepsilon) = A_2 - (A_2 - A_1)\exp(-A_3\varepsilon^{A_4})$	(5)
Swift–Voce (Ref 27)	$\sigma(\varepsilon) = A_1(A_2(A_3 + x)^{A_4}) + (1 - A_5)(A_6 + (A_7 - A_6)\exp(-A_8x))$	(6)
El-Magd (Ref 28)	$\sigma(\varepsilon) = A_1 + A_2\varepsilon + A_3[1 - \exp(-A_4\varepsilon)]$	(7)
Generalized Voce (Ref 29)	$\sigma(\varepsilon) = A_1 + (A_2 + A_3\varepsilon)[1 - \exp(-A_4\varepsilon)]$	(8)

independent constitutive equations shown in Table 1. The material exhibits a small strain hardening rate sensitivity, as discussed in (Ref 6). Based on these observations, we consider the response strain rate-independent and fit the models listed in Table 1 only to the stress–strain curve obtained at the strain rate 8.33×10^{-3} s^{-1}.

It is of interest to observe the evolution of the microstructure during straining, as inferred from the SEM images of etched surfaces. Figure 1 shows SEM images of etched surfaces in the undeformed (0% strain) and deformed (20 and 40% strain) states. The microstructures are clearly different, with the characteristic size of features decreasing continuously upon straining. The grain size remains constant, but the density of twins increases. The thickness of the visible twins decreases from about 800 nm in the undeformed state (Fig. 1a) to about 200 nm at 40% strain (Fig. 1c). Deformation-induced microstructural refinement was observed before in TWIP steels (Ref 38). As the strain increases, the amount of twinned volume of material is controlled by the increase in the number of deformation twins, rather than by the increase in the thickness of existing twins.

The model parameters (i.e., coefficients A_i) resulting from fitting the equations shown in Table 1 to the experimental data are listed in Table 2. The goodness of fit is indicated by the R_σ^2 value which is also reported. It is seen that the goodness of fit is excellent for all models except Hollomon's model. The direct comparison of the measured stress values and those predicted using the various models after fitting is shown in Fig. 4. Clearly, Hollomon's model performs poorly, while the other models reproduce well the experimental data. A similar investigation was performed by Hochholdinger et al. (Ref 19) for 22MnB5 (hot forming of boron alloy). They report that the Hockett/Sherby model, (model (5) in Table 1), provides the best fit to their experimental data, while the Swift–Voce (model (6) in Table 1) overpredicts hardening.

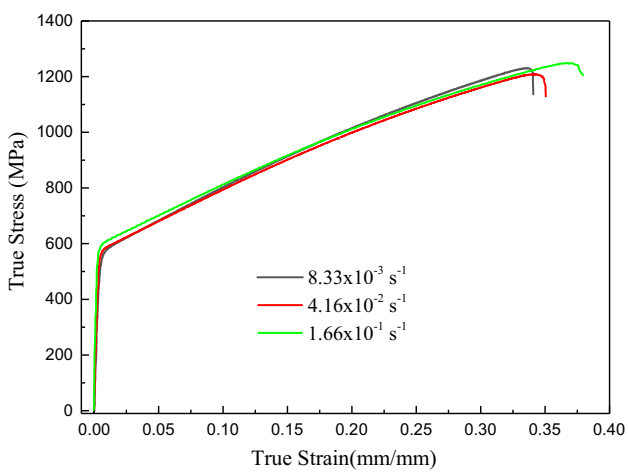

Fig. 3 True stress–true strain curves obtained at three different strain rates

Further, the ability of the models in Table 1, calibrated as discussed above, to predict strain hardening, $\theta = d\sigma/d\varepsilon$, is tested by comparing their predictions with the experimental strain hardening versus strain curve corresponding to the strain rate of 8.33×10^{-3} s^{-1}. The experimental $\theta(\varepsilon)$ along with predictions of all models is shown in Fig. 5. The experimental curve exhibits features that have been broadly discussed in the literature: the initial drop in θ is associated with the rapid dislocation recombination at the onset of plastic deformation. Twinning begins after few percent strain and hence the initial part of the curve is entirely associated with dislocation activity. Once twinning begins, $\theta(\varepsilon)$ levels off and its slope may even become positive in a certain range of strains. This quasi-plateau is considered a central feature of the TWIP effect. The value of the plateau (approximately 2500 MPa, Fig. 5), is very large. Beyond the weakly defined hump observed in the vicinity of 10% strain, $\theta(\varepsilon)$ exhibits a slight, but monotonic decrease.

The comparison of the predicted $\theta(\varepsilon)$ with the experimental curve is a much tougher test for the performance of the constitutive models than the comparison of the stress–strain curves. As seen in Fig. 5, Hollomon's, Swift's and the Power models (models (1), (2) and (3) in Table 1) perform poorly compared with the other models. In addition, none of the proposed models is able to capture the localized hump of the experimental $\theta(\varepsilon)$ curve in the vicinity of 10% strain. Since for this particular material the lack of monotonicity is not pronounced, this discrepancy is of limited importance. In fact, this feature of the $\theta(\varepsilon)$ curve can only be captured by specialized, mechanism-based models, see discussed, for example, in Ref 10.

Contrary to these findings, Collo et al. (Ref 39), who investigated DP steels, reported that the Hollomon model provides the best prediction capability compared to the Pickering, Crussard–Jaoul and Bergstrom models. In another study dedicated to the finite element analysis of advanced high strength steels, the predictions of the Hollomon and Swift models were closest to the experimental data (Ref 40). In another study focusing on 304 and 430 stainless steels, the El-Magd equation provided a very good estimate, while the Ludwik equation provided a poor estimate (Ref 41).

Table 2 Coefficients A_i of models listed in Table 1

Models									
Coefficients	**A1**	**A2**	**A3**	**A4**	**A5**	**A6**	**A7**	**A8**	R_σ^2
(1) Hollomon	1621.011	0.286							0.9594
(2) Power (Ludwik)	520.598	1708.897	0.777						0.9997
(3) Krupskowsky (Swift)	1988.09	0.098	0.5581						0.9998
(4) Voce	2011.653	550.071	1.906						0.9999
(5) Hockett/Sherby	556.61	1825.012	2.43	1.051					0.9999
(6) Swift–Voce	− 0.5888	1988.09	0.098	0.5581	− 0.591	2011.653	550.071	1.906	0.9999
(7) El-Magd	552.066	− 13,289.86	62,283.14	0.2569					0.9999
(8) Generalized Voce	551.139	380.797	1129.934	7.165					0.9999

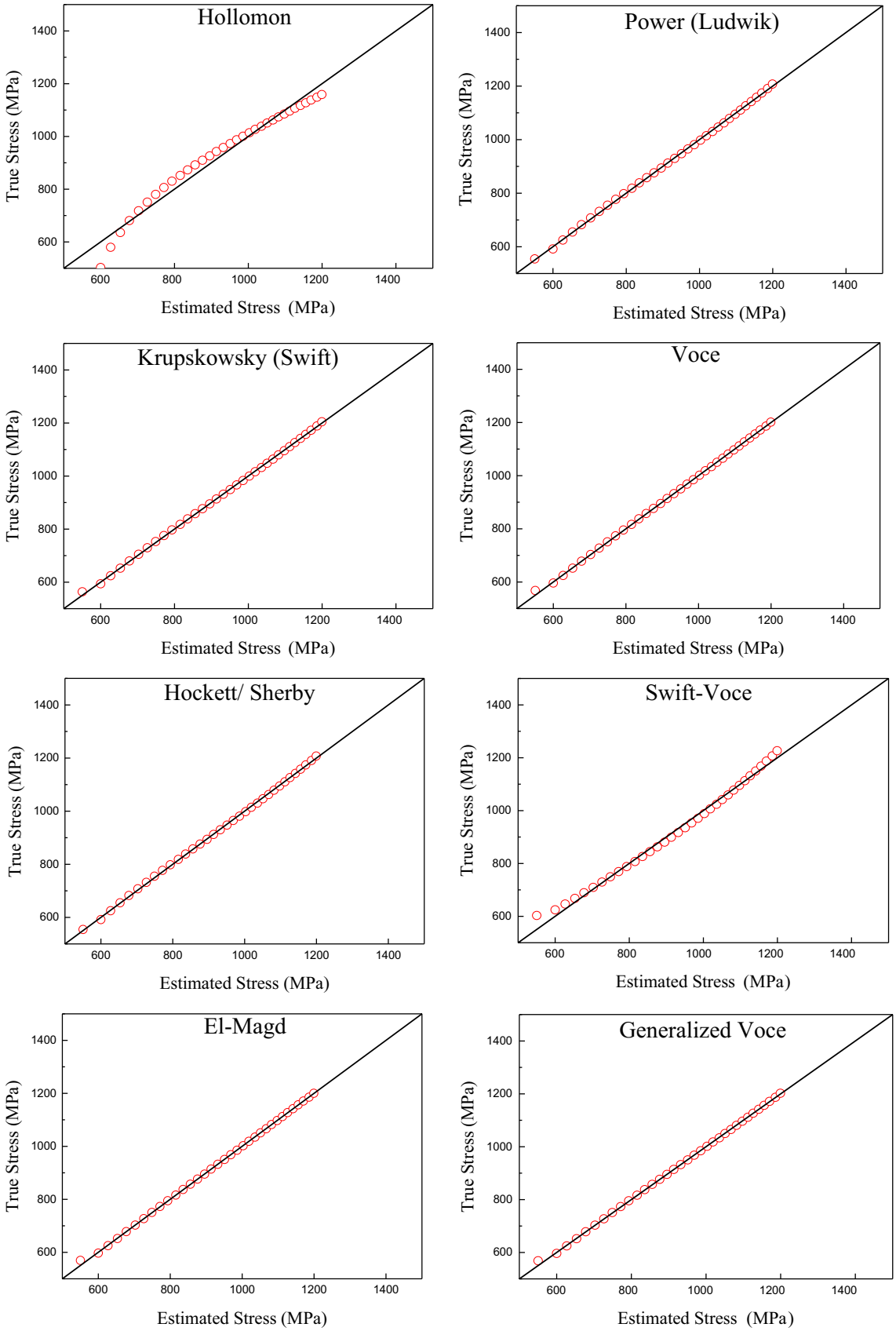

Fig. 4 Comparison of the experimental true stress values with those predicted using models in Table 2

4.2 Prediction of Springback

The ability of the various models considered to predict springback is studied next. To this end, each constitutive model considered was implemented in a finite element model of the configuration shown in Fig. 2. This represents the deformation of a rectangular plate using a 60°V-shaped die. The finite element code DYNAFORM (Ref 43) was used for this purpose.

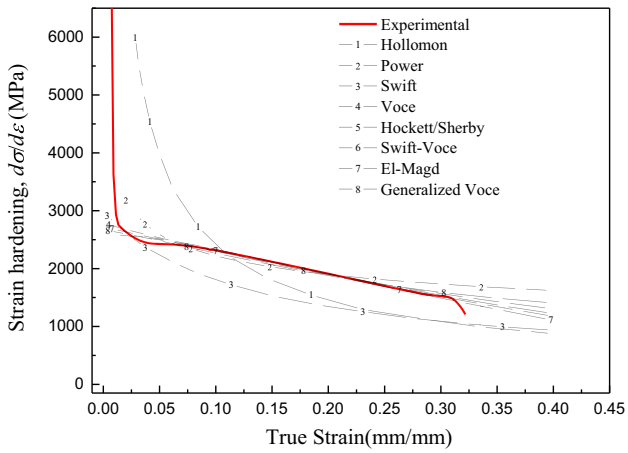

Fig. 5 Strain hardening versus strain for the experimental curve in Fig. 3 corresponding to the strain rate of 8.33×10^{-3} s^{-1} and for all models listed in Table 2

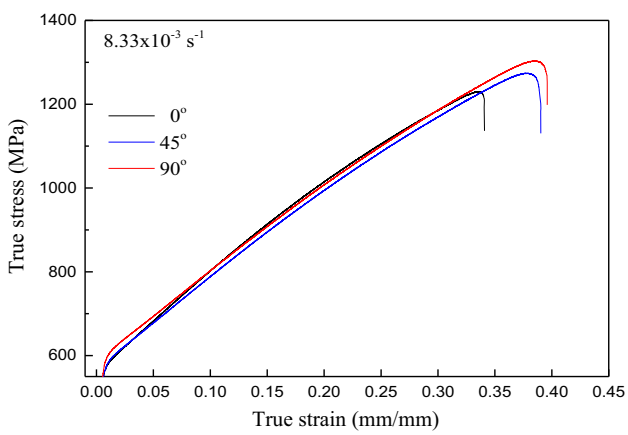

Fig. 6 True stress–true strain curves in different directions

The die and punch were modeled as rigid bodies, and the model was meshed fine enough to eliminate mesh sensitivity. The Belytschko–Tsay shell element with 5 integration points through the thickness was selected in order to simulate the deformation accurately. The friction coefficient was considered to be 0.1 in all simulations; this value is generally assumed in forming models in the literature (Ref 44-46).

Each of the material models was implemented within the MAT_122 material model (Hill48) (Ref 47) of the LS-DYNA material library. This provides the yield surface in the form:

$$2f(\sigma_{ij}) \equiv F(\sigma_y - \sigma_z)^2 + G(\sigma_z - \sigma_x)^2 + H(\sigma_x - \sigma_z)^2 + 2L\tau_{yz}^2 + 2M\tau_{zx}^2 + 2N\tau_{xy}^2 = 1 \quad \text{(Eq 1)}$$

where F, G, H, L, M and N are material constants and x, y and z are the mutual orthogonal axes of orthotropy. Under plane stress condition, the yield surface can be written as:

$$2f(\sigma_{ij}) \equiv (G+H)\sigma_x^2 - 2H\sigma_x\sigma_y + (H+F)\sigma_y^2 + 2N\tau_{xy}^2 = 1. \quad \text{(Eq 2)}$$

constants F, G, H and N can be written in terms of the anisotropy parameters r_0, r_{45}, r_{90} as:

$$F = \frac{r_0}{r_{90}(1+r_{90})}, G = \frac{1}{(1+r_0)}, H = \frac{r_0}{(1+r_0)}, \quad N = \frac{(r_0+r_{90})(1+2r_{45})}{2r_{90}(1+r_0)}. \quad \text{(Eq 3)}$$

the anisotropy parameters for our samples were obtained from separate tensile tests performed in the rolling, diagonal (45°) and transverse directions. The respective stress–strain curves are shown in Fig. 6 (Ref 48). The parameters result: $r_0 = 0.768$, $r_{45} = 1.035$, $r_{90} = 1.274$.

The simulations were performed using a punch velocity of 25 mm/min, which is identical during loading and unloading. The springback angle, defined as the difference between the angle of the die and the final angle of the part, was calculated from each simulation.

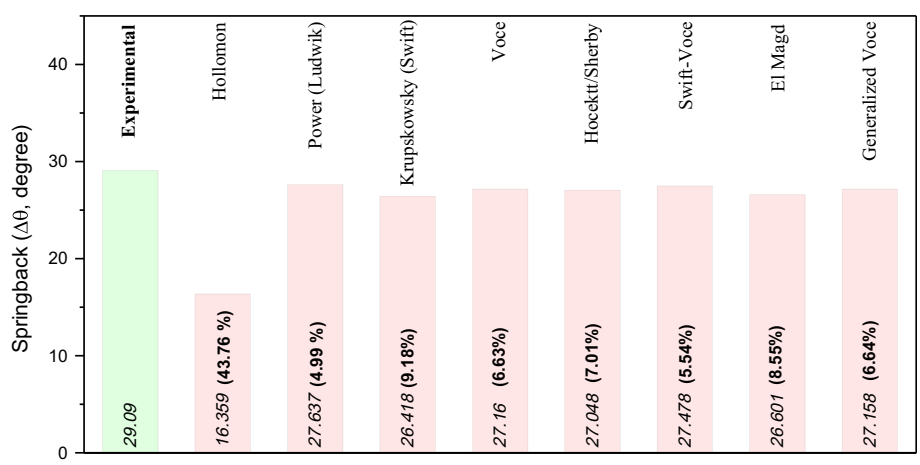

Fig. 7 Springback angle obtained experimentally (leftmost green column) and by modeling using the material models in Table 2 and calibrated parameters. The predicted springback angle is shown numerically along with the percentage error relative to the experimental value (Color figure online)

The reference value for the springback study was obtained experimentally. An experimental setup similar to that in Fig. 2 was used, and the deformation was performed with a punch velocity identical to that reported above and used in the model. The springback angle was measured by optical means, and it was 29.09°.

Figure 7 shows the comparison of this value (leftmost column) with the values obtained with each model in Table 1, with parameters listed in Table 2. The error corresponding to each model is also reported in Fig. 7. As expected, Hollomon's model performs the poorest. The other models provide predictions within 10% from the experimental value. A springback prediction error of 10% and smaller is generally considered acceptable in the literature (Ref 49, 50). Therefore, we conclude that most models in Table 1 lead to acceptable predictions. It is also useful to observe that models calibrated based on uniaxial tension data apply also to bending, which involves both tension and compression. This is applied if the material behavior (e.g., the yield surface) is symmetric in tension and compression, which is the case for the material tested (Ref 7).

The key parameters controlling springback are the elastic modulus, the yield strength, the degree of anisotropy and the hardening behavior (Ref 51). The tool geometry and sheet thickness are also important factors (Ref 52, 53). A material with low elastic modulus exhibits large springback. The magnitude of springback depends on the maximum stress reached during loading, and hence, a material with large strain hardening will present larger springback than a material with small strain hardening and of same yield stress. Therefore, TWIP steels that exhibit vary large hardening rates at all plastic strains and large flow stress values are expected to exhibit large springback. The ability of a model to represent springback accurately depends on its ability to capture the details of the mechanical behavior of the material in the relevant range of stress and strain. The conclusion of practical importance here is that most models predict springback within 10% of the experimental value and hence can be used in forming simulations. This occurs despite the fact that not all of these models provide equally good overall predictions of the stress–strain curve.

5. Conclusion

The ability of several empirical constitutive models to represent the mechanical behavior of TWIP900 high Mn steel was investigated. Eight empirical models were calibrated by fitting to an experimental stress–strain curve. With the exception of Hollomon's model, all models considered can be fitted with reasonable accuracy to the stress–strain curve. However, only the last five models in Table 1 provide an accurate representation of strain hardening. Further, the models were used in conjunction with Hill's yield surface to predict plastic deformation and springback of a plate subjected to bending in a V-shaped die. All models except Hollomon's provided predictions within 10% of the springback value obtained experimentally for the same configuration. These results guide model selection in simulations of plastic deformation of this type of TWIP steel.

Conflict of Interest

The authors declare that they have no conflict of interest.

References

1. R.W. Neu, Performance and Characterization of TWIP Steels for Automotive Applications, *Mater. Perform. Charact.*, 2013, **2**(1), p. 244-284. https://doi.org/10.1520/MPC20130009
2. O. Grässel, L. Krüger, G. Frommeyer, and L.W. Meyer, High strength Fe-Mn-(Al, Si) TRIP/TWIP Steels Development—Properties—Application, *Int. J. Plast*, 2000, **16**(10), p 1391–1409
3. I. Gutierrez-Urrutia, S. Zaefferer, and D. Raabe, The Effect of Grain Size and Grain Orientation on Deformation Twinning in a Fe-22wt.% Mn-0.6wt.% C TWIP Steel, *Mater. Sci. Eng., A*, 2010, **527**(15), p 3552–3560
4. S. Kılıç and F. Öztürk, Comparison of Performances of Commercial TWIP900 and DP600 Advanced High Strength Steels in Automotive İndustry, *J. Fac. Eng. Arch. Gazi Univ.*, 2016, **31**(3), p 567–578
5. S. Kilic, F. Ozturk, T. Sigirtmac, and G. Tekin, Effects of Pre-strain and Temperature on Bake Hardening of TWIP900CR Steel, *J. Iron. Steel Res. Int.*, 2015, **22**(4), p 361–365
6. A. Bintu, G. Vincze, C.R. Picu, A.B. Lopes, J.J. Grácio, and F. Barlat, Strain Hardening Rate Sensitivity and Strain Rate Sensitivity in TWIP Steels, *Mater. Sci. Eng., A*, 2015, **629**, p 54–59
7. K. Chung, K. Ahn, D.-H. Yoo, K.-H. Chung, M.-H. Seo, and S.-H. Park, Formability of TWIP (Twinning İnduced Plasticity) Automotive Sheets, *Int. J. Plast*, 2011, **27**(1), p 52–81
8. T.A. Lebedkina, M.A. Lebyodkin, J.P. Chateau, A. Jacques, and S. Allain, On the Mechanism of Unstable Plastic Flow in an Austenitic FeMnC TWIP Steel, *Mater. Sci. Eng., A*, 2009, **519**(1–2), p 147–154
9. S. Curtze and V.T. Kuokkala, Dependence of Tensile Deformation Behavior of TWIP Steels on Stacking Fault Energy, Temperature and Strain Rate, *Acta Mater.*, 2010, **58**(15), p 5129–5141
10. D.R. Steinmetz, T. Jäpel, B. Wietbrock, P. Eisenlohr, I. Gutierrez-Urrutia, A. Saeed-Akbari, T. Hickel, F. Roters, and D. Raabe, Revealing the Strain-Hardening Behavior of Twinning-İnduced Plasticity Steels: Theory, Simulations, Experiments, *Acta Mater.*, 2013, **61**(2), p 494–510
11. A. Dumay, J.P. Chateau, S. Allain, S. Migot, and O. Bouaziz, Influence of Addition Elements on the Stacking-Fault Energy and Mechanical Properties of an Austenitic Fe-Mn-C Steel, *Mater. Sci. Eng., A*, 2008, **483**, p 184–187
12. J.M. Choung and S.R. Cho, Study on True Stress Correction from Tensile Tests, *J. Mech. Sci. Technol.*, 2008, **22**(6), p 1039–1051
13. Y. Lin, K.M. Hsu, and P.K. Lee, The Application of Flow Stress Model to Sheet Metal Forming Simulation, *China Steel Techn. Rep.*, 2010, **23**, p 31–35
14. S.K. Paul, Predicting the Flow Behavior of Metals Under Different Strain Rate and Temperature Through Phenomenological Modeling, *Comput. Mater. Sci.*, 2012, **65**, p 91–99
15. A. Smith, Z. Chen, J.Y. Lee, M.G. Lee, and R.H. Wagoner, Effective Method for Fitting Complex Constitutive Equations, *Int. J. Plast*, 2014, **58**, p 100–119
16. K. Roll, Simulation of Sheet Metal Forming–Necessary Developments in the Future, in *Proceedings of Numisheet Conference*, Interlaken, Switzerland (2008), pp. 3–11
17. S.-I. Oh, J.-K. Lee, J.-J. Kang, and J.-P. Hong, Applications of Simulation Techniques to Sheet Metal Forming Processes, *Met. Mater.*, 1998, **4**(4), p 583–592
18. K. Roll, Advanced Simulation Techniques-Exceeding Reality?, *Mater. Sci. Technol. Assoc. Iron Steel Technol.*, 2007, **2**, p 1288
19. B. Hochholdinger, H. Grass, A. Lipp, P. Hora, and B.M.W.A.G. Munich, Determination of Flow Curves by Stack Compression Tests and Inverse Analysis for the Simulation of Hot Forming, in *7th European LS-DYNA Conference* (2009)
20. S. Dziallach, W. Bleck, M. Blumbach, and T. Hallfeldt, Sheet Metal Testing and Flow Curve Determination under Multiaxial Conditions, *Adv. Eng. Mater.*, 2007, **9**(11), p 987–994
21. A. Nasser, A. Yadav, P. Pathak, and T. Altan, Determination of the Flow Stress of Five AHSS Sheet Materials (DP 600, DP 780, DP 780-CR, DP 780-HY and TRIP 780) Using the Uniaxial Tensile and the Biaxial Viscous Pressure Bulge (VPB) Tests, *J. Mater. Process. Technol.*, 2010, **210**(3), p 429–436
22. S.K. Paul, Predicting the Flow Behavior of Metals Under Different Strain Rate and Temperature Through Phenomenological Modeling, *Comput. Mater. Sci.*, 2012, **65**, p 91–99

23. H.B. Wang, M. Wan, and Y. Yan, Effect of Flow Stress-Strain Relation on Forming Limit of 5754O Aluminum Alloy, *Trans. Nonferrous Metals Soc. China*, 2012, **22**(10), p 2370–2378
24. D. Escobar, S.S.F. de Ferreira, and D.B. Santos, Martensite Reversion and Texture Formation in 17Mn-0.06C TRIP/TWIP Steel After Hot Cold Rolling and Annealing, *J. Mater. Res. Technol.*, 2015, **4**(2), p 162–170
25. G. Sun, S. Hu, Y. Gao, and W. Chen, Influence of Direct Annealing Heat Treatment on the Mechanical Properties of As-Casting TWIP Steels, *J. Mater. Eng. Perform.*, 2017, **26**(5), p 1981–1985
26. M. Eskandari, M.A. Mohtadi-Bonab, A. Zarei-Hanzaki, A.G. Odeshi, and J.A. Szpunar, High-Resolution EBSD Study of Adiabatic Shear Band and Neighboring Grains After Dynamic Impact Loading of Mn-Steel Used in Vehicle Structure, *J. Mater. Eng. Perform.*, 2016, **25**(4), p 1611–1620
27. P. Lan and J. Zhang, Tensile Property and Microstructure of Fe-22Mn-0.5C TWIP Steel, *Mater. Sci. Eng., A*, 2017, **707**, p 373–382
28. P.D. Nezhadfar, A. Rezaeian, and M.S. Papkiadeh, Softening Behavior of a Cold Rolled High-Mn Twinning-Induced Plasticity Steel, *J. Mater. Eng. Perfor.*, 2015, **24**(10), p 3820–3825
29. A. Grajcar, M. Kciuk, S. Topolska, and A. Płachcińska, Microstructure and Corrosion Behavior of Hot-Deformed and Cold-Strained High-Mn Steels, *J. Mater. Eng. Perform.*, 2016, **25**(6), p 2245–2254
30. P. Russo Spena, F. D'Aiuto, P. Matteis, and G. Scavino, Dissimilar Arc Welding of Advanced High-Strength Car-Body Steel Sheets, *J. Mater. Eng. Perform.*, 2014, **23**(11), p 3949–3956
31. M. Iker, D. Gaude-Fugarolas, P. Jacques, and F. Delannay, Combination of TWIP Effect and Hardening by Carbide Precipitation in Austenitic Steels with High Manganese and Carbon Contents, in *Proceedings of Thermec 2006: International Conference on processing & manufacturing of advanced materials*. The Minerals, Metals, Materials Society (TMS), Vancouver (2006)
32. B.H. Song, Y.-D. Park, J. Park, I. Choi, K. Cho, and Y.K. Lee, Effect of Deformation Twin on Mechanical Properties of Lean Manganese Twinning Induced Plasticity (TWIP) Steels at Quasi-Static Strain Rate, in *The Twenty-third International Offshore and Polar Engineering Conference* (International Society of Offshore and Polar Engineers, 2013)
33. O. Holovenko, M. Ienco, E. Pastore, M. Pinasco, P. Matteis, G. Scavino, and D. Firrao, Microstructural and Mechanical Characterization of Welded Joints on İnnovative High-Strength Steels, *La Metallurgia Italiana*, 2013, **3**(1), p 3–12
34. H. Schumann and K. Goodknecht, Metallographıc Proof of Epsılon Martensıte ın Austenıtıc Steels, *Prak Metallogr.*, 1966, **3**(4), p 147–153
35. K. Phiu-on, Deformation Mechanisms and Mechanical Properties of Hot Rolled Fe-Mn-C-(Al)-(Si) Austenitic Steels. (2008), http://publications.rwth-aachen.de/record/50402/files/Phiu_on_Kriangyut.pdf. Accessed 1 May 2016
36. R.C. Picu and A. Majorell, Mechanical Behavior of Ti-6Al-4 V at High and Moderate Temperatures—Part II: Constitutive Modeling, *Mater. Sci. Eng., A*, 2002, **326**(2), p 306–316
37. N. Origin (OriginLab, MA) 2015
38. J.-E. Jin and Y.-K. Lee, Strain hardening behavior of a Fe–18Mn–0.6C–1.5Al TWIP steel, *Mater. Sci. Eng., A*, 2009, **527**(1), p 157–161
39. V. Colla, M. De Sanctis, A. Dimatteo, G. Lovicu, A. Solina, and R. Valentini, Strain hardening behavior of dual-phase steels, *Metall Mat Trans A*, 2009, **40**(11), p 2557–2567
40. Y.-K. Lin, K.-M. Hsu, and P.-K. Lee, The Application of Flow Stress Model to Sheet Metal Forming Simulation, *China Steel Techn. Rep.*, 2010, **23**, p 31–35
41. B. Sener and M. Yurci, Comparison of Quasi-Static Constitutive Equations and Modeling of Flow Curves for Austenitic 304 and Ferritic 430 Stainless Steels, *Acta Phys. Polon. A*, 2017, **131**(3), p 605–607
42. DYNAFORM, Complete Die System Simulation Solution Software (2015), https://www.eta.com/inventium/dynaform. Accessed 1 May 2015
43. P. Chen and M. Koç, Simulation of Springback Variation in Forming of Advanced High Strength Steels, *J. Mater. Process. Technol.*, 2007, **190**(1), p 189–198
44. M. Kadkhodayan and I. Zafarparandeh, On the Relation of Equivalent Plastic Strain and Springback in Sheet Draw Bending, *Int. J. Mater. Form.*, 2008, **1**(1), p 141–144
45. J.-Y. Lee, J.-W. Lee, M.-G. Lee, and F. Barlat, An Application of Homogeneous Anisotropic Hardening to Springback Prediction in Pre-strained U-Draw/Bending, *Int. J. Solids Struct.*, 2012, **49**(25), p 3562–3572
46. J.O. Hallquist, LS-DYNA Keyword User's Manual, *Livermore Softw. Technol. Corp.*, 2007, **970**, p 299
47. S. Kilic and F. Ozturk, Evaluation of Formability Under Different Deformation Modes for TWIP900 Steel, *J. Eng. Mater. Technol.*, 2017, **139**(3), p 031001–031008
48. X. Jingjing, W. Xiumei, Z. Ping, W. Yimin, C. Nianyi, L. Wencong, Springback Prediction in Sheet Metal Forming Combined Finite Element Method with Date Mining Technique (2002), https://www.ansys.com/-/media/ansys/corporate/resourcelibrary/conference-paper/2002-int-ansys-conf-5.pdf. Accessed 1 June 2016
49. K.I. Patel, Evaluation of Springback Prediction Capability Using Uniform Pure Bending (2006), https://soar.wichita.edu/xmlui/bitstream/handle/10057/365/t06053.pdf?sequence=3&isAllowed=y. Accessed 1 July 2016
50. T. Trzepiecinski and H.G. Lemu, Effect of Computational Parameters on Springback Prediction by Numerical Simulation, *Metals*, 2017, **7**(9), p 380
51. D. Zhu, Newest Progress on the Springback's Study of Plate Forming, *J. Plast. Eng.*, 2000, **1**, p 11–17
52. Y. Moon, S. Kang, J. Cho, and T. Kim, Effect of Tool Temperature on the Reduction of the Springback of Aluminum Sheets, *J. Mater. Process. Technol.*, 2003, **132**(1), p 365–368
53. T. Trzepiecinski and H.G. Lemu, Prediction of Springback in V-die Air Bending Process by Using Finite Element Method, in *MATEC Web of Conferences*, 2017. https://doi.org/10.1051/matecconf/201712103023. Accessed 1 September 2017